

# Atomic-scale insights into surface species of electrocatalysts in three dimensions

T. Li<sup>1,2,6</sup>, O. Kasian<sup>1,6</sup>, S. Cherevko<sup>1,3</sup>, S. Zhang<sup>1</sup>, S. Geiger<sup>1</sup>, C. Scheu<sup>1</sup>, P. Felfer<sup>4</sup>, D. Raabe<sup>1</sup>, B. Gault<sup>1,5\*</sup> and K. J. J. Mayrhofer<sup>1,5\*</sup>

**The topmost atomic layers of electrocatalysts determine the mechanism and kinetics of reactions in many important industrial processes, such as water splitting, chlor-electrolysis or fuel cells. Optimizing the performance of electrocatalysts requires a detailed understanding of surface-state changes during the catalytic process, ideally at the atomic scale. Here, we use atom probe tomography to reveal the three-dimensional structure of the first few atomic layers of electrochemically grown iridium oxide, an efficient electrocatalyst for the oxygen evolution reaction. We unveil the formation of confined, non-stoichiometric Ir–O species during oxygen evolution. These species gradually transform to IrO<sub>2</sub>, providing improved stability but also a decrease in activity. Additionally, electrochemical growth of oxide in deuterated solutions allowed us to trace hydroxy-groups and water molecules present in the regions of the oxide layer that are favourable for the oxygen evolution and iridium dissolution reactions. Overall, we demonstrate how tomography with near-atomic resolution advances the understanding of complex relationships between surface structure, surface state and function in electrocatalysis.**

With increasing energy demand and related environmental concerns, access to affordable and sustainable energy is the cornerstone of the world's increasing prosperity and economic growth. Water electrolysis for production of hydrogen serves as a key technology in the renewable energy cycle. But increasing the efficiency and longevity of water electrolyzers remains a serious challenge, predominantly owing to limitations in the performance of the anode electrocatalysts at which the oxygen evolution reaction (OER) takes place<sup>1,2</sup>. The reaction itself triggers changes in the electrode surface composition, leading as a rule to the deterioration of the electrocatalytic properties during operation<sup>3,4</sup>. Optimization of the electrocatalyst's performance can arise only from a detailed understanding of the relationship between the surface composition of the electrode and its electrochemical behaviour.

In the acidic conditions of proton-exchange membrane water electrolyzers, iridium and its oxides exhibit the best combination of high activity towards OER<sup>5–7</sup> and long-term stability<sup>8–11</sup>. However, the electrocatalytic properties of Ir oxide electrodes vary greatly depending on their fabrication route: for example, electrochemically formed oxides generally show higher electrocatalytic activity than those formed by thermal oxidation of metallic Ir (refs <sup>12,13</sup>). The surface structure of Ir oxides synthesized by chemical routes or thermal decomposition of respective Ir-based precursors has been extensively investigated by X-ray-based techniques<sup>14,15</sup>, including *ex situ*<sup>16</sup> and *in situ* X-ray photoelectron spectroscopy (XPS)<sup>17,18</sup>. The structure and composition of electrochemically formed oxides on the surface of metallic Ir are much less understood. Moreover, during the OER, both undergo considerable changes<sup>19</sup>, and, up to now, the mechanisms underpinning these transformations and their influence on the activity and stability have remained a subject of intense debate<sup>17,18</sup>, mainly because of technical limitations of the surface science techniques currently used in electrochemistry<sup>20</sup>.

The resulting knowledge gap regarding the nature of the active species on the surface Ir oxides, which might form locally with different structure and can be only a few atomic layers thick, hinders the further development of high-performance OER electrocatalysts.

Here, we characterize the temporal evolution of the topmost atomic layers of Ir oxide formed on model 100-nm-thick pure Ir films by anodic electrochemical oxidation in the conditions used for the OER (see Methods). Advanced activity–stability analyses performed by scanning flow cell connected to an inductively coupled plasma mass spectrometer (SFC-ICP-MS) were combined with high-end near-atomic-scale characterization by atom probe tomography (APT), (scanning) transmission electron microscopy ((S)TEM), electron energy-loss spectroscopy (EELS) and X-ray photoelectron spectroscopy (XPS). Additionally, to resolve hydroxy-groups by APT in the electrochemically grown oxides, proton-free deuterated electrolytes were used to avoid overlap with residual hydrogen from the ultra-high-vacuum chamber<sup>21</sup>. Our study reveals that the surface layer formed at the beginning of the electrolysis consist of non-stoichiometric Ir–O species mixed with hydroxy-groups and water molecules, providing high electrocatalytic activity. These metastable Ir–O species gradually transform into IrO<sub>2</sub>, which yields a decrease in activity and an increase in stability. With a view of the 3D compositional distribution, we provide unique experimental evidence of the chemical species residing at or near the outermost surface of iridium oxides and their transformation at near-atomic scale, which is critical for understanding the interplay between composition, activity and stability in electrocatalysis.

## Results

**Activity, stability and surface electronic structure.** To form oxide films, metallic Ir electrodes were anodically polarized at 1 mA cm<sup>–2</sup> for 4, 69 or 120 h. These durations were selected on the basis of

<sup>1</sup>Max-Planck-Institut für Eisenforschung GmbH, Düsseldorf, Germany. <sup>2</sup>Institute for Materials & Zentrum für Grenzflächendominierte Höchstleistungswerkstoffe (ZGH), Bochum, Germany. <sup>3</sup>Helmholtz-Institute Erlangen-Nürnberg for Renewable Energy (IEK-11), Forschungszentrum Jülich GmbH, Erlangen, Germany. <sup>4</sup>Institute for General Materials Properties, Department of Materials Science, Friedrich-Alexander-Universität Erlangen-Nürnberg, Erlangen, Germany. <sup>5</sup>Department of Chemical and Biological Engineering, Friedrich-Alexander-Universität Erlangen-Nürnberg, Erlangen, Germany. <sup>6</sup>These authors contributed equally: T. Li, O. Kasian. \*e-mail: [b.gault@mpie.de](mailto:b.gault@mpie.de); [k.mayrhofer@fz-juelich.de](mailto:k.mayrhofer@fz-juelich.de)

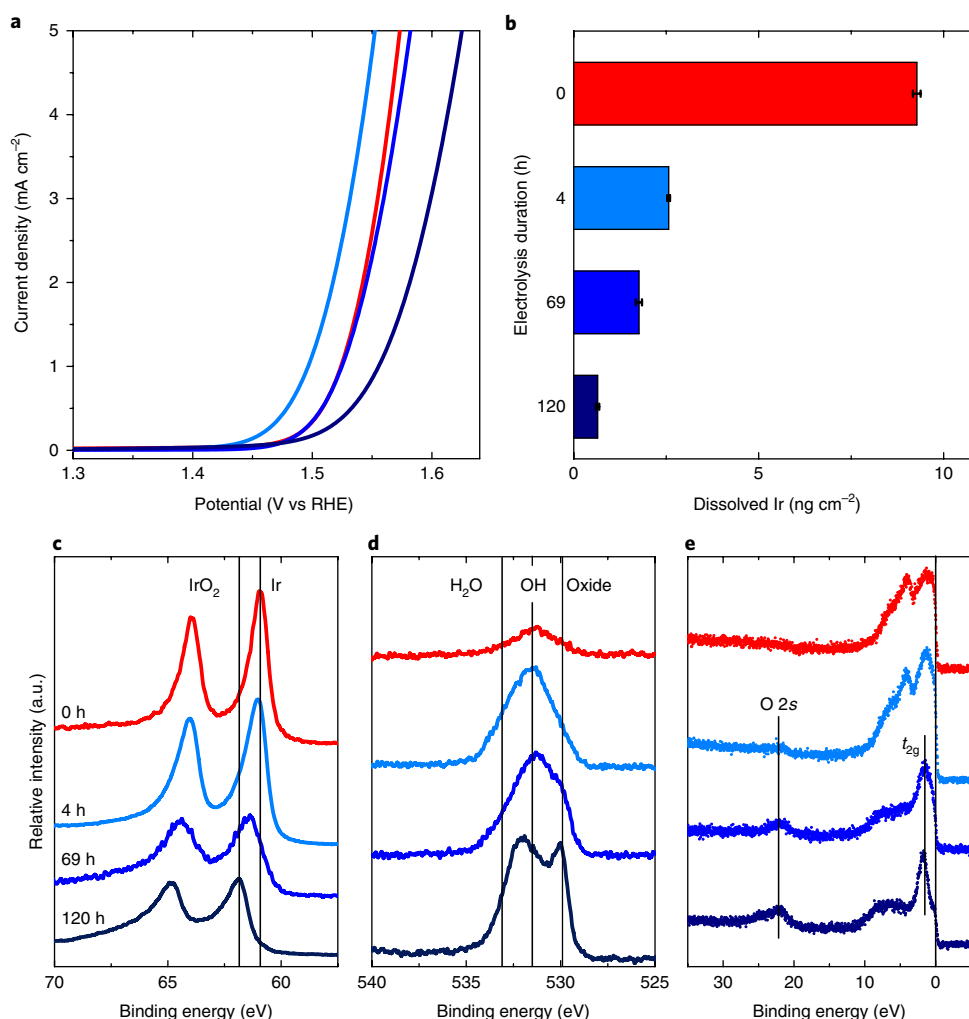


**Fig. 1 | Activity and stability of electrochemically formed Ir oxides and their surface electronic state.** **a**, Anodic polarization curves of as-prepared metallic Ir (red) and its electrochemically grown oxides (shades of blue). Colour gradient from light to dark blue indicates an increase in electrolysis duration from 4 h to 69 h and 120 h. **b**, Amount of dissolved Ir measured online during the corresponding potential scans from 1.2 V<sub>RHE</sub> to a potential corresponding to 5 mA cm<sup>-2</sup> with a scan rate 10 mV s<sup>-1</sup> in 0.1 M HClO<sub>4</sub>. **c**, X-ray photoelectron spectra of Ir 4f level. **d**, X-ray photoelectron spectra of O 1s level. **e**, X-ray photoelectron valence-band spectra. The error bars in **b** represent standard deviation calculated on the basis of three identical measurements. The solid vertical line at zero corresponds to the Fermi level.

marked changes in the electrocatalytic performance of such oxide films occurring during this timeframe (Supplementary Fig. 1 and Supplementary Note 1). An anodic sweep of potential was performed after each polarization step using SFC-ICP-MS, in order to compare their respective activity and stability. The electrocatalytic activity towards OER is derived from the current–voltage (*I*–*V*) curves as the value of potential at current density of 5 mA cm<sup>-2</sup>. A lower potential observed at a given current density implies a higher activity. Figure 1a reveals that oxides formed during approximately the first 4 h of electrolysis exhibit a higher activity towards OER than does a freshly prepared metallic film. Further increase in electrolysis duration leads to deterioration of the catalytic activity. Simultaneously, online ICP-MS was used to analyse the amount of electrochemically dissolved Ir during OER, which is directly related to the material's stability as summarized in Fig. 1b. The oxide formation due to anodic polarization results in a progressively lower dissolution rate. Interestingly, the Ir oxide formed in 4 h does not show the expected trend of decreasing stability with increasing activity. Considering the density of Ir atoms in the oxide lattice, it can be estimated that 320 ng cm<sup>-2</sup> corresponds to one monolayer. The measured dissolution rate of the least stable metallic Ir is in the

range of a few per cent of a monolayer, which may result in considerable degradation of proton-exchange membrane electrolyzers over the device's lifetime<sup>22</sup>.

**Morphology of the surface oxides.** To address the gradual change in activity and stability of the Ir oxide, we consider its electronic structure, morphology and composition more closely. XPS allows access to the average electronic state of approximately 100 μm × 100 μm × 5 nm of a surface. Narrow scans of the Ir 4f, O 1s levels and a valence-band region from the metallic Ir and electrochemically pretreated electrodes are presented in Fig. 1c–e, respectively. The formation of IrO<sub>2</sub> after 120 h (Fig. 1c) is confirmed by the shift of the Ir 4f<sub>7/2</sub> peak from 60.9 eV corresponding to metallic Ir to 61.6 eV, typically assigned to Ir<sup>IV</sup> (ref. 17). Simultaneously, an increase in the contribution from lattice oxygen (529.8 eV) O 1s spectra is observed as the electrolysis proceeds, which is indicative of the growth of the oxide on the surface of metallic Ir (Fig. 1d). Additionally, all electrochemically formed samples show strong contributions from OH groups as well as H<sub>2</sub>O in the O 1s spectra. In line with these observations, the valence-band spectra of Ir show noticeable changes with increasing duration of the OER (Fig. 1e). Similar to metallic

Ir, the oxide film formed during the first 4 h exhibits a structureless 5d band extended to about 10 eV below the Fermi level. After 69 h, a strong  $t_{2g}$  emission centred at 1.8 eV (the two darker blue curves in Fig. 1e) appears, corresponding to five electrons in the valence band<sup>20</sup>, typical for the octahedral coordination of Ir atoms in the oxide lattice. However, the overall broad structure of the  $t_{2g}$  peak is different from that observed for rutile IrO<sub>2</sub> prepared by thermal oxidation (Supplementary Fig. 2 and Supplementary Note 2), indicating that rutile IrO<sub>2</sub> has not yet fully formed. The oxide film grown after 120 h has a well-defined valence-band structure, indicated by sharp  $t_{2g}$  peaks, that corresponds to rutile IrO<sub>2</sub> (dark blue curve in Fig. 1e). The change in electron density at the Fermi level of these three oxides can be interpreted as the gradual transformation of metallic Ir into rutile IrO<sub>2</sub> during the OER. Although this macroscopically explains the improvement in stability, the enhancement of activity during the first stages of the anodic oxidation remains unresolved.

The fine-scale morphology of the electrochemical oxide film was observed by aberration-corrected annular bright-field (ABF) STEM combined with EELS. To protect the surface from the energetic ion beam during specimen preparation (see Methods), Cr was sputter-deposited at room temperature onto the sample. This thin Cr layer also provides a marker for the location of the interface (Fig. 2a, Supplementary Fig. 3 and Supplementary Note 3). Figure 2b is a representative ABF image of the 69 h oxide layer, revealing an oxide layer of uneven thickness grown on the columnar Ir grains. The oxygen EELS mapping in Fig. 2c further illustrates that the electrochemical oxide is in the form of spheres of diameter 7–8 nm on the Ir surface.

**Distribution of individual atoms and composition of the surface oxides.** The inherent scale of the main features of the oxide films renders them difficult to analyse fully in the 2D projected image of the specimen accessible by TEM, as several features of interest can overlap. Accurate quantification of oxide compositions is also affected by a possible reduction of the Ir oxides by the electron beam<sup>23</sup>. We therefore turned to APT, a mass-spectrometry technique with subnanometre spatial resolution<sup>24</sup>, to map the distribution of individual atoms within the surface oxides in 3D. APT data take the form of a 3D point cloud, in which every point represents a single ion detected and elementally identified. Figure 3a–h displays top-down and side views of APT data obtained from the analyses of the as-deposited Ir film and the different oxide films. Figure 3a shows variations in the point-density that are typical for small grains and grain boundaries<sup>25</sup>: the as-deposited Ir film is nanocrystalline, with a grain size of about 10 nm. The Ir surface is oxygen-free (Fig. 3b; confirmed by mass spectra in Supplementary Fig. 4

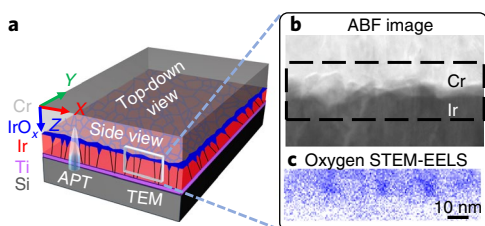
and Supplementary Note 4). After anodic polarization for 4 h, the electrochemical oxide film is only a few nanometres thick and covers the surface unevenly, with accelerated growth selectively at grain boundaries (Fig. 3c,d). Selective oxidation on the grain boundaries has also been observed during the thermal oxidation of Ir (ref. <sup>26</sup>) and platinum-group metal alloys<sup>27</sup>. As the anodic oxidation time increases to 69 h, the number density of oxide particles increases, and they grow from a size of about 2–3 nm to 6–8 nm, as observed in Fig. 3e,f. We can now confirm that the oxide islands, observed by STEM/EELS in Fig. 2c, are formed at the triple or quadruple junctions between grains. After anodic oxidation for 120 h, the oxide particles tend to coalesce into a thicker oxide film (approximately 8–10 nm in thickness) in Fig. 3g,h.

The composition of the electrochemical oxide evolves, as revealed by composition profiles in Fig. 3i–k calculated along the arrows labelled 1, 2 and 3 in Fig. 3d,f, and h respectively. The oxygen concentration in the electrochemical oxide layers gradually increases as the anodic oxidation proceeds. The composition profiles along the arrows marked 1\*, 2\* and 3\*, plotted in Supplementary Fig. 5 (see details in Supplementary Note 5), indicate that each oxide particle within the same oxide film has a slightly different oxygen content. For example, the O:Ir ratio in region 1 (Fig. 3i) is about 0.81, whereas it is 0.96 in region 1\* (Supplementary Fig. 5a). The average atomic ratios of O to Ir within the topmost surface of the oxide film measured from at least three APT datasets are summarized in Table 1 (see details in Supplementary Fig. 6, Supplementary Table 1 and Supplementary Note 5). After anodic oxidation for 4 h, the average O:Ir ratio is about 0.5. It increases to 1.6 on average after anodic polarization for 69 h and reaches approximately 2.4 at 120 h, in line with XPS results (Fig. 1c,e). However, the level of detail accessible by APT allows us to expose highly localized formation of oxide clusters, predominantly at grain boundaries, which are sometimes only a few tens of atoms in size and show varying stoichiometry (Fig. 3) that could not be revealed by ‘macroscopic’ XPS measurements.

The possible presence of water and hydroxy-groups in the electrochemically grown oxides was then examined. A proton-free, deuterated electrolyte was used for the oxide preparation to avoid overlap with the residual hydrogen from the ultra-high-vacuum chamber in APT<sup>21</sup>. A comparison of the mass spectra from the hydrogenated and deuterated electrochemical oxide (region 2 in Fig. 3f) in Supplementary Fig. 7 confirms that deuterated oxygen-containing molecular ions (OD<sup>+</sup>, D<sub>2</sub>O<sup>+</sup>) are detected (see details in Supplementary Note 6). Figure 3d reveals that most hydroxy-groups are present in the electrochemical oxide particles after anodic oxidation for 4 h, whereas water appears as background (that is, randomly distributed) in both the Cr capping layer and the Ir oxide layer (confirmed by Supplementary Fig. 8 and Supplementary Note 6). In comparison, at 69 h, both the water molecules and hydroxy-groups are concentrated within the oxide islands (Fig. 3f). More interestingly, after anodic polarization for 120 h, water and hydroxy-groups cover only the surface of the electrochemical oxide, as seen in Fig. 3h.

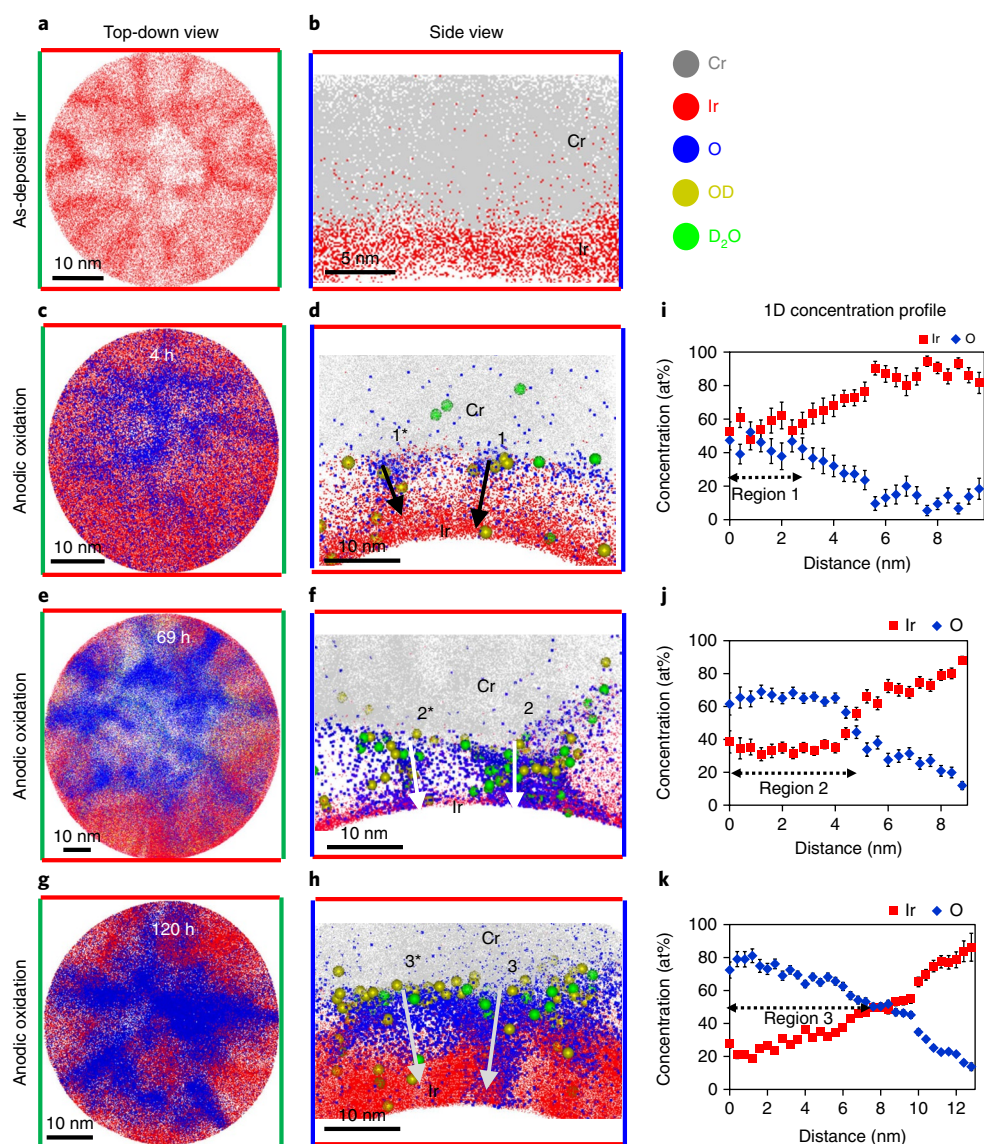
## Discussion

Figure 4 schematically summarizes the temporal evolution of the Ir oxides and their electrocatalytic performance during the OER. The observed gradual alterations of the activity and stability of the Ir oxide (Fig. 1a,b) can be correlated with the stoichiometry of the Ir–O species at the surface and in the near-surface regions (Table 1 and Fig. 3). During the first 4 h of electrolysis, both activity and stability improve, whereas the oxide films formed by longer oxidation lead to an expected trend of deterioration in the activity with increasing stability<sup>4,28</sup>. Formation of oxide clusters at triple junctions during the first 4 h apparently plays an important role in OER electrocatalysis on Ir, improving both stability and activity. At the beginning of polarization, the oxide clusters are small, improving



**Fig. 2 | Schematic of the sample and edge-on surface oxide morphology of Ir after exposure to anodic oxidation for 69 h.** **a**, Schematic diagram illustrating the structure of thin films. From bottom to top: Si wafer, 15 nm Ti, 80 nm Ir, Ir oxide and 200 nm Cr as a protective layer. X–Z (red–blue) and X–Y (red–green) present the side view and top-down view for 3D APT reconstruction in Fig. 3. **b**, ABF image and **c**, STEM-EELS mapping of O K edge in the black-dashed region in the corresponding ABF-STEM image.





**Fig. 3 | APT data of as-deposited Ir film and Ir oxides formed by anodic oxidation for 4 h, 69 h and 120 h. a–h,** Top-down view and side view of APT reconstructions of as-deposited Ir (**a,b**), and anodic oxidation for 4 h (**c,d**), 69 h (**e,f**), and 120 h (**g,h**). **i–k,** One-dimensional concentration profiles from the regions along the arrows labelled 1, 2 and 3 in **d, f** and **h**, respectively (for 1\*, 2\* and 3\*, see Supplementary Fig. 5). The error bars for the concentration were calculated from  $\sqrt{c(100-c)/N}$ , where  $c$  is the concentration (in at%) and  $N$  is the total number of atoms within a bin of the profile.

**Table 1 | Average O:Ir ratios in electrochemical oxides**

Anodic oxidation time (h)	Averaged O:Ir ratio
4	$0.5 \pm 0.3$
69	$1.6 \pm 0.1$
120	$2.4 \pm 0.4$

the OER kinetics. With the aid of APT, we observe locally a thin (<5 nm) metastable oxide with an Ir to O ratio of 1:1 that forms during the first 4 h of anodic polarization. This contrasts with the common perception of a mixture of Ir<sup>0</sup> and Ir<sup>IV</sup> species<sup>15,17,29</sup> on the surface of electrochemically formed Ir oxide. The formation of IrO possibly results from orientation-dependent oxidation kinetics<sup>26,30</sup> and hence represents a transient, metastable state in the formation of rutile IrO<sub>2</sub>. The adsorption of oxygen-containing radicals on non-stoichiometric Ir–O would be energetically favoured in

comparison to IrO<sub>2</sub> (ref. <sup>31</sup>). Thus, the increase in activity during the first 4 h can be correlated to the number of sites containing non-stoichiometric Ir–O species within the topmost surface layers as the dominant active species for the OER. Further increase in electrolysis duration to 69 h results in partial oxidation of metastable Ir–O species towards IrO<sub>2</sub> and their complete transformation into rutile IrO<sub>2</sub> after 120 h. These observations agree with macroscopic XPS data (Fig. 1c–e) and explain the simultaneous decrease in electrocatalytic activity (Fig. 1a).

Interestingly, the Ir oxide formed during the first 4 h shows higher activity and lower dissolution than the as-prepared metallic Ir film. Further stability improvements during anodic polarization up to 120 h are less pronounced. This suggests that the triple junctions contribute considerably to the dissolution of metallic Ir, whereas further formation of precursor oxide clusters after 4 h hinders the dissolution. Along with that, the lower stability of metallic Ir also results from its direct dissolution during the oxidation, which becomes less probable with increasing oxide coverage<sup>32</sup>.

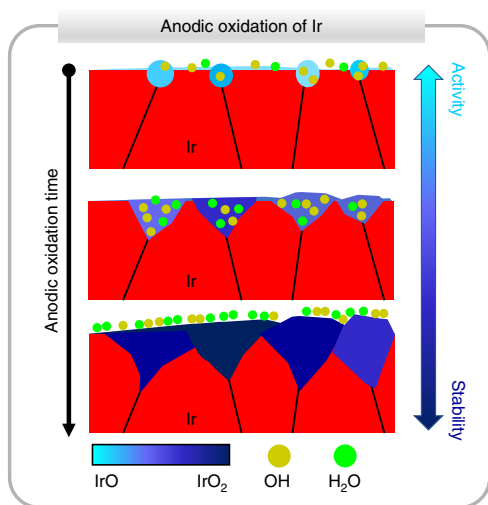


**Fig. 4 | Schematic representation of the gradual changes observed during anodic polarization of Ir under OER conditions.** At the beginning of electrolysis, small oxide particles consisting of non-stoichiometric Ir–O species along with loosely bound hydroxy-groups and water molecules form at the triple junctions and grain boundaries. The O:Ir ratio varies across different oxide particles. As the anodic polarization proceeds, the average O:Ir ratio in the surface oxide layer increases from 1 to 2, giving rise to a decrease in activity and an increase in stability.

In turn, further oxidation and the variation in the Ir–O stoichiometry impede Ir dissolution and lead to progressive improvement in stability, as shown in Fig. 1b. As the OER proceeds, stoichiometric IrO<sub>2</sub> eventually forms as the thermodynamically stable phase in these conditions.

In addition, isotope-labelled APT experiments show hydroxy-groups and water molecules distributed within the surface or matrix of anodically formed oxides (Fig. 3d,f,h). Hydroxy-groups and water molecules within the oxide layer can be considered as ‘fingerprints’ of the Ir oxidation reaction and indicate regions where the corresponding reaction takes place. At the beginning of the electrolysis, hydroxy-groups are mainly localized in the oxide clusters as observed in Fig. 3d and f, whereas, after 120 h, only the surface of the oxide shows noticeable hydration (Fig. 3h).

To summarize, gradual changes in the composition of surface species during the OER on Ir can be directly linked to activity and stability. As the anodic polarization proceeds, the average O to Ir ratio in the surface layer rises from  $0.5 \pm 0.3$  at 4 h to  $1.6 \pm 0.1$  at 69 h and  $2.4 \pm 0.4$  after 120 h. Simultaneously, the activity towards the OER decreases, while the stability seemingly improves (Fig. 1a,b and Supplementary Fig. 1). Substoichiometric Ir–O species with a 1:1 O to Ir ratio are formed on the surface of the electrode during the first 4 h of electrolysis. Such species are metastable and obviously have a high affinity for oxygen adsorption to form a thermodynamically stable state. As the adsorption step becomes favoured, the OER accelerates. The amount of Ir–O species decreases as they partially transform into IrO<sub>2</sub>, as observed for an Ir electrode that was polarized for 69 h. As a result of a decrease of active species, the activity deteriorates. According to recent reports<sup>13,32</sup>, for electrochemically polarized electrodes lower activity towards the OER results in stability improvement. Finally, after 120 h of anodic polarization, the entire electrode’s surface is covered with IrO<sub>2</sub>, resulting in a further decrease in activity and higher stability. Overall, the composition of the topmost atomic layers and, thus, the activity–stability behaviour of the Ir electrode is determined by the ratio between the rates of the oxidation, dissolution and oxygen evolution reactions.

## Conclusions

Our study provides atomic-scale insights into the atomistic structure and composition of the near-surface regions of electrochemically grown Ir oxide catalysts and their influence on OER activity and stability. In the future, the strength of our advanced characterization approach, showcased by OER as an important model reaction, can be extended to resolve surface species or active sites of other (electro-)catalytic systems. This will aid the understanding of reaction mechanisms, resulting in the development of new atomistic design strategies for high-performance catalysts.

## Methods

**Sample preparation.** Thin films of Ir were deposited on smooth substrates of single-crystal Si wafers (100) with 1.5  $\mu\text{m}$  thermal SiO<sub>2</sub> using magnetron sputtering (BesTec GmbH, Germany). Before mounting the sample into the deposition chamber, we cleaned the substrates in an ultrasonic bath with acetone and isopropanol and dried them with compressed dry air. The base vacuum before deposition was  $2 \times 10^{-6}$  Pa. A 20-nm Ti adhesion layer was deposited on the substrate before Ir evaporation. The 3-inch target of Ir (99.9%, Evochem, Germany) was pre-cleaned by sputtering against closed shutters before deposition. Argon (99.999%) was used as the sputter gas, and the chamber pressure was regulated to 0.5 Pa at room temperature. Deposition was performed at constant substrate rotation of 20 r.p.m. and sputtering power of 100 W for 60 minutes. The resulting thickness of the obtained coating was approximately 100 nm.

Electrochemical oxides were prepared by anodic polarization of the iridium film at 1 mA cm<sup>−2</sup> for 4, 69 or 120 h in a solution of 0.1 M DClO<sub>4</sub> prepared by dilution of a concentrated acid (68 wt% in D<sub>2</sub>O, Sigma-Aldrich) in D<sub>2</sub>O (99.9 at%, Armar GmbH, Leipzig, Germany). Before APT probing, freshly prepared samples were rinsed with ultrapure D<sub>2</sub>O, placed in a desiccator filled with Ar and transferred into the high-vacuum chamber. The samples were then coated with a 200-nm layer of Cr by using electron-beam evaporation of (99.999%) pure material at 90 W with a deposition rate of about 2.5 Å s<sup>−1</sup> at a vacuum level of  $2 \times 10^{-6}$  Pa.

**Electrochemical measurements.** All electrochemical measurements were carried out in 0.1 M HClO<sub>4</sub> solution prepared by dilution of concentrated acid (Suprapur 70% HClO<sub>4</sub>, Merck, Germany) in ultrapure water (PureLab Plus system, Elga, 18 M $\Omega$  cm, total organic carbon <3 ppb). The electrolyte was purged with Ar during the measurements.

The measurements were performed using a scanning flow cell connected to an ICP-MS (NexION 300X, Perkin Elmer) to examine the stability and activity towards the OER of different materials in real time. The set-up has been described in detail previously<sup>33</sup>. All data presented have been normalized to the geometric area of the working electrode ( $1 \times 10^{-2}$  cm<sup>2</sup>), assuming that the roughness of the thin-film sputtered electrodes is small. A graphite rod was used as the counter-electrode, and saturated Ag/AgCl (Metrohm, Germany) was used as the reference electrode. All potentials reported are referred to the reversible hydrogen electrode (RHE) potential, which was separately measured on each day of an experiment. A Gamry (Reference 600, USA) potentiostat was used to control potential or current. To ensure the accuracy of the ICP-MS measurements, the device was calibrated on each experiment day before the electrochemical measurements were conducted. Additionally, a solution containing 10  $\mu\text{g l}^{-1}$  Re was used as an internal standard to ensure stable performance of the mass spectrometer.

The following experimental protocol was applied in all OER studies. The potential was swept from  $E = 1.20 \text{ V}_{\text{RHE}}$  to a value corresponding to a current density of 5 mA cm<sup>−2</sup> at a scan rate of 10 mV s<sup>−1</sup>. At least three measurements were conducted for each sample to ensure reproducibility of the results. The electrocatalytic activity towards OER was defined as a potential value at a current density of 5 mA cm<sup>−2</sup> (Fig. 1a). The stability was measured online by quantifying the amount of electrochemically dissolved Ir during the OER using the scanning flow cell connected to the ICP-MS (Fig. 1b).

**X-ray photoelectron spectroscopy.** XPS measurements were carried out (Quantera II, Physical Electronics, Chanhassen, MN, USA) by applying a monochromatic Al K $\alpha$  X-ray source (1,486.6 eV) operating at 15 kV and 25 W. The binding energy scale was referenced to the C 1s signal at 285.0 eV. Analysis of the spectra was carried out with the Casa XPS (<http://www.casaxps.com/>) software.

**Scanning transmission electron microscopy.** A focused ion beam (FIB) lift-out technique was used to prepare TEM samples using a FEI Helios 600 Nanolab FIB/scanning electron microscope. To protect the surface oxides from potential damage by the ion beam, a Cr layer was deposited on the Ir surfaces by electron-beam physical vapour deposition (Fig. 2a). The high-resolution STEM experiments were carried out in a probe-corrected FEI-Titan operated at 300 kV. A sub-Ångstrom probe with a convergence semi-angle of 24 mrad was used, and 50 pA current was scanned at 10  $\mu\text{s}$  per pixel. High-angle annular dark field and ADF images were recorded by using corresponding detector ranges with collection of semi-angles of 73–352 mrad and 8–16 mrad, respectively. EELS was acquired by the post-column

energy filter Quantum ERS (GATAN) at 1 eV dispersion and 0.1 s per pixel. The oxygen K-edge intensity map was integrated between 520 and 540 eV after subtracting the background by power-law fitting.

**Atom probe tomography.** Needle-shaped APT specimens were prepared by means of a site-specific lift-out procedure using a FEI Helios 600 Nanolab FIB/scanning electron microscope. A 200-nm-thick protective Cr layer was coated on top of the Ir by electron-beam physical vapour deposition to protect the surface oxides (Fig. 2a). The APT experiments were conducted on a CAMECA LEAP 5000 XS instrument equipped with an ultraviolet laser with a spot size of 2 µm and a wavelength of 355 nm. The ion detection efficiency of this state-of-the-art microscope using the currently highest resolving multi-channel detector plate is about 80%. Data were acquired in laser pulsing mode at a specimen temperature of 60 K, with a target evaporation rate of five ions per 1,000 pulses, a pulsing rate of 200 kHz and a laser pulse energy of 60 pJ. The APT data were reconstructed and analysed using the commercial IVAS 3.6.14 software. For each oxide, three datasets were obtained for further data analysis.

**Data availability.** The data that support the findings of this study are available from the corresponding and first authors upon reasonable request.

Received: 1 July 2017; Accepted: 15 February 2018;

Published online: 26 March 2018

## References

- Stamenkovic, V. R., Strmcnik, D., Lopes, P. P. & Markovic, N. M. Energy and fuels from electrochemical interfaces. *Nat. Mater.* **16**, 57–69 (2017).
- Seh, Z. W. et al. Combining theory and experiment in electrocatalysis: insights into materials design. *Science* **355**, eaad4998 (2017).
- Grimaud, A. et al. Activation of surface oxygen sites on an iridium-based model catalyst for the oxygen evolution reaction. *Nat. Energy* **2**, 16189 (2016).
- Grimaud, A. et al. Activating lattice oxygen redox reactions in metal oxides to catalyse oxygen evolution. *Nat. Chem.* **9**, 457–465 (2017).
- McCorry, C. C. et al. Benchmarking hydrogen evolving reaction and oxygen evolving reaction electrocatalysts for solar water splitting devices. *J. Am. Chem. Soc.* **137**, 4347–4357 (2015).
- McCorry, C. C., Jung, S., Peters, J. C. & Jaramillo, T. F. Benchmarking heterogeneous electrocatalysts for the oxygen evolution reaction. *J. Am. Chem. Soc.* **135**, 16977–16987 (2013).
- Reier, T., Oezaslan, M. & Strasser, P. Electrocatalytic oxygen evolution reaction (OER) on Ru, Ir, and Pt catalysts: a comparative study of nanoparticles and bulk materials. *ACS Catal.* **2**, 1765–1772 (2012).
- Beni, G., Schiavone, L. M., Shay, J. L., Dautremont-Smith, W. C. & Schneider, B. S. Electrocatalytic oxygen evolution on reactively sputtered electrochromic iridium oxide films. *Nature* **282**, 281–283 (1979).
- Cherevko, S. et al. Oxygen and hydrogen evolution reactions on Ru, RuO<sub>2</sub>, Ir, and IrO<sub>2</sub> thin film electrodes in acidic and alkaline electrolytes: a comparative study on activity and stability. *Catal. Today* **262**, 170–180 (2016).
- Seitz, L. C. et al. A highly active and stable IrO<sub>2</sub>/SrIrO<sub>3</sub> catalyst for the oxygen evolution reaction. *Science* **353**, 1011–1014 (2016).
- Willing, E., Massué, C., Schlögl, R. & Willinger, M. -G. Identifying key structural features of IrO<sub>2</sub> water splitting catalysts. *J. Am. Chem. Soc.* **139**, 12093–12101 (2017).
- Spöri, C., Kwan, J. T. H., Bonakdarpour, A., Wilkinson, D. P. & Strasser, P. Stabilitätsanforderungen von Elektrokatalysatoren für die Sauerstoffentwicklung: der Weg zu einem grundlegenden Verständnis und zur Minimierung der Katalysatordegradation. *Angew. Chem. Int. Ed.* **129**, 6088–6117 (2017).
- Danilovic, N. et al. Activity–stability trends for the oxygen evolution reaction on monometallic oxides in acidic environments. *J. Phys. Chem. Lett.* **5**, 2474–2478 (2014).
- Minguzzi, A. et al. Easy accommodation of different oxidation states in iridium oxide nanoparticles with different hydration degree as water oxidation electrocatalysts. *ACS Catal.* **5**, 5104–5115 (2015).
- Reier, T. et al. Molecular insight in structure and activity of highly efficient, low-Ir Ir–Ni oxide catalysts for electrochemical water splitting (OER). *J. Am. Chem. Soc.* **137**, 13031–13040 (2015).
- Kötz, R., Neff, H. & Stucki, S. Anodic iridium oxide films: XPS-studies of oxidation state changes and O<sub>2</sub> evolution. *J. Electrochem. Soc.* **131**, 72–77 (1984).
- Pfeifer, V. et al. The electronic structure of iridium oxide electrodes active in water splitting. *Phys. Chem. Chem. Phys.* **18**, 2292–2296 (2016).
- Sanchez Casalongue, H. G. et al. In situ observation of surface species on iridium oxide nanoparticles during the oxygen evolution reaction. *Angew. Chem. Int. Ed.* **53**, 7169–7172 (2014).
- Reier, T., Nong, H. N., Teschner, D., Schlögl, R. & Strasser, P. Electrocatalytic oxygen evolution reaction in acidic environments—reaction mechanisms and catalysts. *Adv. Energy Mater.* **7**, 1601275 (2017).
- Wertheim, G. K. & Guggenheim, H. J. Conduction-electron screening in metallic oxides: IrO<sub>2</sub>. *Phys. Rev. B* **22**, 4680–4683 (1980).
- Chen, Y.-S. et al. Direct observation of individual hydrogen atoms at trapping sites in a ferritic steel. *Science* **355**, 1196–1199 (2017).
- Alia, S. M. et al. Activity and durability of iridium nanoparticles in the oxygen evolution reaction. *J. Electrochem. Soc.* **163**, F3105–F3112 (2016).
- Massue, C. et al. High-performance supported Ir-oxohydroxide water oxidation electrocatalysts. *ChemSusChem* **10**, 1943–1957 (2017).
- Gault, B. & Moody, M. P. & Cairney, J. M. & Ringer, S. P. *Atom Probe Microscopy* Vol. 160 (Springer Science & Business Media, New York, 2012).
- Moody, M. P., Tang, F., Gault, B., Ringer, S. P. & Cairney, J. M. Atom probe crystallography: characterization of grain boundary orientation relationships in nanocrystalline aluminium. *Ultramicroscopy* **111**, 493–499 (2011).
- Fortes, M. A. & Ralph, B. The growth of oxide on field-ion specimens of iridium. *Proc. R. Soc. Lond. A* **307**, 431–448 (1968).
- Li, T., Bagot, P. A. J., Marquis, E. A., Tsang, S. C. E. & Smith, G. D. W. Characterization of oxidation and reduction of Pt–Ru and Pt–Rh–Ru alloys by atom probe tomography and comparison with Pt–Rh. *J. Phys. Chem. C* **116**, 17633–17640 (2012).
- Binner, T. et al. Thermodynamic explanation of the universal correlation between oxygen evolution activity and corrosion of oxide catalysts. *Sci. Rep.* **5**, 12167 (2015).
- Geiger, S. et al. Activity and stability of electrochemically and thermally treated iridium for the oxygen evolution reaction. *J. Electrochem. Soc.* **163**, F3132–F3138 (2016).
- Özer, E., Spöri, C., Reier, T. & Strasser, P. Iridium(111), iridium(110), and ruthenium(0001) single crystals as model catalysts for the oxygen evolution reaction: insights into the electrochemical oxide formation and electrocatalytic activity. *ChemCatChem* **9**, 597–603 (2016).
- Chen, D., Chen, C., Baiyee, Z. M., Shao, Z. & Ciucci, F. Nonstoichiometric oxides as low-cost and highly-efficient oxygen reduction/evolution catalysts for low-temperature electrochemical devices. *Chem. Rev.* **115**, 9869–9921 (2015).
- Kasian, O., Grote, J.-P., Geiger, S., Cherevko, S. & Mayrhofer, K. J. J. The common intermediates of oxygen evolution and dissolution reactions during water electrolysis on iridium. *Angew. Chem. Int. Ed.* **57**, 2488–2491 (2018).
- Klemm, S. O. et al. Time and potential resolved dissolution analysis of rhodium using a microelectrochemical flow cell coupled to an ICP-MS. *J. Electroanal. Chem.* **677**–**680**, 50–55 (2012).

## Acknowledgements

T.L. and O.K. acknowledge the Alexander von Humboldt Foundation. S.Z. and C.S. thank the German Science Foundation within the Priority Programme SPP 1613 (DFG SCHE 634/12-2).

## Author contributions

K.J.J.M. and B.G. initiated the project. O.K. prepared Ir oxide films, performed the electrochemical and XPS measurements and carried out data analysis. T.L. prepared the APT and TEM samples, conducted the APT experiment and analysed the APT data. S.Z. carried out the TEM experiment. T.L., O.K., B.G., S.C., D.R. and K.J.J.M. wrote the paper. All authors discussed the results and their interpretation.

## Competing interests

The authors declare no competing interests.

## Additional information

**Supplementary information** is available for this paper at <https://doi.org/10.1038/s41929-018-0043-3>.

**Reprints and permissions information** is available at [www.nature.com/reprints](http://www.nature.com/reprints).

**Correspondence and requests for materials** should be addressed to B.G. or K.J.J.M.

**Publisher's note:** Springer Nature remains neutral with regard to jurisdictional claims in published maps and institutional affiliations.